Materials Advances

ROYAL SOCIETY OF CHEMISTRY

PAPER

View Article Online
View Journal | View Issue

Cite this: *Mater. Adv.*, 2026, 7, 4093

Nanoparticle-based superchain networks formed by the side-by-side self-assembly of soft magnetite nanorods

Madeleine Alexandra Schaefer,[a] Sebastian Polarz[a] and Irene Morales*[ab]

Mesophases are structures of higher order formed by anisotropic building blocks, the most prominent case being thermotropic molecular liquid crystals. The self-assembly of anisotropic inorganic nanoparticles is attracting significant interest to design novel and complex functional materials, obtaining superstructures resembling these mesophases. A key question is whether, and how, magnetic interactions between magnetic nanorods affect the self-assembly process compared to their non-magnetic counterparts. Existing studies often rely on polycrystalline magnetic nanorods or silica shell coatings, thus reducing the magnetic interactions and shape anisotropy and introducing additional electrostatic repulsion. Here, we present the synthesis of single-crystalline magnetite nanorods stabilized only by organic ligands, allowing for unhindered magnetic interactions, showing that the aspect ratio can be precisely adjusted by the ligand choice. Assembling these nanorods revealed the formation of unusual superchain structures in ferrite nanorods, distinct from the classical nematic or cholesteric phases. In the assembled samples, the superchain formation results in an antiparallel dipole–dipole alignment of neighboring nanorods attaching side-by-side to reduce the magnetostatic energy through flux closure. At a sufficient length of the superchains, percolation takes place, forming a network enclosing cavities containing nanorods in a disordered state. Longer nanorods exhibit a higher tendency for superchain formation, leading to a denser network with a higher fraction of nanorods included into the superchains. The resulting assembly preserves the ferrimagnetic-superparamagnetic behaviour of the building blocks while exhibiting direction-dependent magnetic properties. Without the need of a silica shell to obtain this alignment, the close interparticle contact offers exciting perspectives for magnetoelectrical applications.

Received 15th October 2025,
Accepted 16th March 2026

DOI: 10.1039/d5ma01195g

rsc.li/materials-advances

Introduction

Particle-based materials have gained interest in recent years as they can exhibit synergistic properties stemming from the programmed superposition of defined building blocks in a periodic superstructure. Denser packings represent states of overall higher entropy due to volume exclusion of solvate molecules, which induces the self-assembly and structuration process.[1,2] Direction-dependent properties and possible collective characteristics prove to be important in technological applications.[3] For non-magnetic materials, understood here as those without ferro-, ferri- or superparamagnetic behaviour, lots of studies have reported the formation of particle-based materials by using nanodots (isotropic in all three spatial directions), nanorods, and nanoplates as building blocks.[1,2,4] For nanorods, the resulting phases are often compared to thermotropic liquid crystal phases formed by hard colloids, which depending on the order can be: isotropic/liquid (random orientation, random position), nematic (random position, fixed orientation), or smectic (fixed position only in plane, fixed orientation).[1] A phase frequently observed in nanorods is smectic, examples include Au,[5] TiO_2,[6] CdSe/CdS,[7] ZnO,[8,9] and many more. The fundamental interactions between nanoparticles include depletion attraction, capillary, van der Waals (attractive), and electrostatic (repulsive) forces.[10,11]

The superstructures formed by magnetic nanoparticles deviating from an isotropic shape[12] are particularly interesting due to their magnetic properties and the additional dipolar interactions at play during assembly. The most prominent example are nanorods, showcasing high shape anisotropy. The assembly of magnetic nanoparticles into ordered superstructures offers fascinating perspectives towards the adjustment of magnetic features such as coercivity, effective saturation

---

[a] *Institute of Inorganic Chemistry, Leibniz University Hannover, Callinstrasse 9, 30167, Hannover, Germany. E-mail: irene.morales@aca.uni-hannover.de*

[b] *Cluster of Excellence PhoenixD (Photonics, Optics and Engineering- Innovation Across Disciplines), Leibniz University Hannover, 30167 Hannover, Germany*

magnetization, non-linear magnetic phenomena, carrier mobility, magneto-optical, or magneto-electrical properties.[13–16] An external magnetic field can not only be applied to the prepared material, but it can also be used for the modulation of the self-assembly process itself. Combined with the interparticle interactions, this can lead to intriguing structuration effects.[17] Another good example can be found in the field of magnetic hyperthermia, where the formation of nanoparticle chains increases the heating efficiency of the system.[4]

From the set of well-known nanocrystals with fully understood magnetic properties, ferrite particles, in particular those made of Fe_3O_4 (magnetite), represent a prime spot. Magnetite is a widely used and researched ferrimagnetic material with a high magnetic saturation ($M_S \approx 92$ emu g^{-1}) in bulk.[18] Related to the cubic crystal system of magnetite (Spinel structure; space group $Fd\bar{3}m$), crystalline particles with very high quality, different sizes, and isotropic shapes, such as cubes or cuboctahedrons, are readily available.[19,20] In the superparamagnetic regime (below $\approx$ 25 nm),[19] particles show zero coercivity (H_C) and zero remanence (M_R) at temperatures above their blocking temperature (T_B). Magnetite nanoparticles (MagNPs) are applied successfully in a variety of fields. Examples are active colloids,[21–23] biomedicine,[19,24–26] catalysis,[27–29] and environmental remediation[19,25,30] The assembly of MagNPs into chains has been reported in great detail.[31–36] Nanocubes could be arranged into helical structures[37] and mesocrystals.[38–41] Nano-octahedrons are known for their assembly in 2D monolayers[42] and 3D superlattices.[42]

Considering the extensive work on self-assembly of non-magnetic nanorods mentioned before, it is highly interesting to investigate the differences that the additional magnetic interactions make when using magnetite nanorods (MagNR) as building blocks. The following aspects have to be considered: the synthesis of ferrite nanorods is less established compared to the quasi-spherical NPs, and a fine control over the aspect ratio of the MagNRs is desirable. To properly obtain information about the influence of magnetic interactions into the self-assembly in comparison to their non-magnetic counterparts, silica coating should be avoided, leading to organic ligand-stabilized and single-crystalline MagNRs.

A dominant method for the preparation of MagNRs is the synthesis of a different iron oxide first, either hematite (Fe_2O_3; rhomohedral, $R3c$) or β-FeOOH (monoclinic, $I4/m$), because it is much easier to break symmetry compared to the cubic crystal system of magnetite.[43] A controlled reduction then yields Fe_3O_4 while the shape of the rods is retained. Various procedures have been presented in the literature,[43] such as hydrothermal,[44] electrochemical,[45] or wet chemical methods.[46] A wide range of nanorod lengths is available, ranging from 45 nm[47,48] and 80[49] nm to over 200 nm.[50,51] Some reports describe sizes even larger than 1 μm.[44,45] The reported methods also have disadvantages. It has been shown that structural integrity remains higher after chemical reduction if the iron oxide nanorods are coated with a silica shell beforehand.[52,53] Furthermore, it is very difficult to obtain monocrystalline nanorods. Polycrystallinity, on the other hand, has negative effects on the magnetic properties due to the occurrence of grain boundaries, and also makes it difficult to compare one sample to the other.

The post-preparative reduction route is only one reason for the dominance of silica-coated MagNRs found in the literature. The coating, in particular if thicker, reduces the contribution of the magnetic dipole–dipole interactions, becoming less important in their assembly process. The silica shell (negatively charged) contributes additional electrostatic repulsion.[54,55] The latter factors are important as they reduce the tendency for irreversible agglomeration processes, which have been observed for as-synthesized, ligand-stabilized MagNRs.[56] Furthermore, the silica shell leads to rounding of the edges of the MagNRs.[57] This could lead to a situation where the interaction profile of the particles is much less anisotropic than expected.[57] In a paper published in 2021,[16] the authors minimized the thickness of the silica shell and presented an intriguing example of the huge potential of MagNR assembly driven by an external magnetic field. In their work, depending on the aspect ratio and the application of an external magnetic field, a highly ordered but non-close-packed yet hard-contact tetragonal particle-based supercrystal was created. Additionally, hematite spindles (<400 nm, weakly ferromagnetic) have been reported to arrange into nematic like bundles in weak magnetic fields.[58] Theoretical simulations of hard magnetic nanorods are available and could predict the behaviour of non-coated magnetite nanorods. Dense 2D structures are predicted to be obtained by antiparallel-oriented magnetic dipole moments, as this reduces the magnetostatic energy.[59]

The current paper aims at the synthesis of monocrystalline MagNR with an adjustable size and their self-assembly into superstructures. The self-assembly of the particles is investigated in detail, as well as the magnetic properties of the new materials.

Results and discussion

Synthesis of single-crystalline MagNR with adjustable size

Our method is based on a solvothermal approach reported in ref. 60. The thermal decomposition of pentacarbonyl iron ($Fe(CO)_5$) in octanol/hexadecylamine as a solvent and iron oleate as a stabilizing ligand allows the direct synthesis of MagNRs, and a subsequent reduction step is not necessary. Two modifications were made to improve the quality of the obtained nanorods and to allow size control and are presented in the following.

(i) A prehydrolysis procedure was introduced by heating the organic ligands, oleic acid and hexadecylamine, in 1-octanol; see also the experimental part. We found that the polydispersity of the MagNR length becomes significantly narrower, as shown in Fig. 1a, obtaining particles with a PDI of 0.095 (9.5%). Decreasing polydispersity is an important factor, as it can hugely influence the order in nanorod-based superstructures, as reported in the case of semiconducting materials.[8] The nanorod size and morphology were investigated using TEM (transmission electron microscopy), by determining the width,

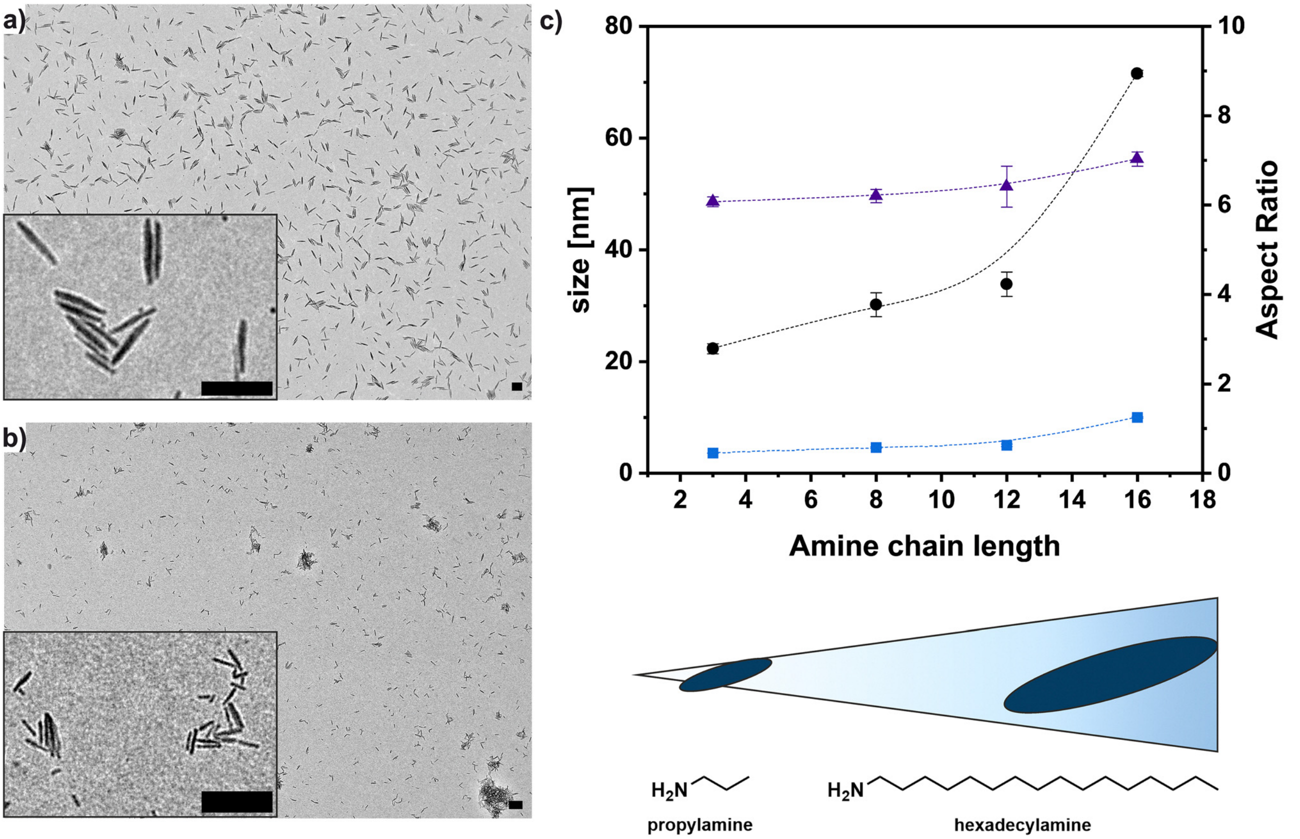

Fig. 1 TEM images (scale bar: 100 nm) of the resulting magnetite nanorods using (a) hexadecylamine, (b) propylamine and (c) length (black circles), width (blue rectangles) and resulting aspect ratio (purple triangles) correlated to the amine chain length. The aspect ratio was calculated for each nanorod and at least 100 nanorods were measured for each sample and the resulting distributions were fitted using a lognormal distribution to obtain the average length, width and aspect ratio. TEM images of the nanorods with other chain lengths are shown in Fig. S1. The size distributions are shown in Fig. S2.

length, and aspect ratio of at least 100 nanorods and then fitted to a lognormal distribution (Table 1 and Fig. S2). The length of MagNR prepared using hexadecylamine is 72 nm, and the width is 9 nm. (ii) We replaced the hexadecyl amine used in the synthesis with alternative amines. Amines with shorter C-chain lengths lead to smaller particles (Fig. 1c). The shortest amine, propylamine, reduced the length of the nanorods to 22 nm (Fig. 1b). We observe that the size reduction is directly related to the C-chain length of the used amines. Furthermore, we introduced oleyl amine as a ligand, which can also be used to reduce the size of the obtained nanorods, which was previously reported for isotropic particles.[61] The aspect ratio and polydispersity of all obtained nanorods is similar to those obtained with hexadecylamine, which is important for further use.

Table 1 Overview of the properties of the obtained nanorods

Amine used	Length/[nm]	Width/[nm]	Aspect Ratio	Organic Content ICP-OES[a]/ [wt%]
Hexadecylamine	71.57 ± 0.53	9.99 ± 0.12	7.03 ± 0.16	20.77
Dodecylamine	33.83 ± 2.19	5.00 ± 0.23	6.41 ± 0.46	16.55
Octylamine	30.16 ± 2.13	4.59 ± 0.14	6.20 ± 0.15	16.38
Propylamine	22.29 ± 0.87	3.59 ± 0.02	6.07 ± 0.11	13.37
Oleylamine	31.41 ± 1.08	5.45 ± 0.11	5.59 ± 0.20	17.36

[a] ICP-OES data evaluation is detailed in SI A.

X-ray diffraction (XRD) was used to characterize the iron oxide phase. In comparison with literature data for magnetite (cif: 1513301[62]), it can be seen that the main phase in the obtained XRD data (Fig. 2a and Fig. S5) fits the expected peaks for magnetite, although it is generally hard to distinguish from maghemite in XRD measurements. The presence of magnetite as the main phase can be further confirmed by XPS and by the observation of the Verwey transition, as investigated through SQUID magnetometry. XPS measurements confirmed the magnetite phase inside the nanorods, but showed oxidation in the surface layer (Fig. S3). High-resolution transmission electron microscopy (HR-TEM, Fig. 2b and Fig. S4) was used to confirm both the phase and growth direction, and additionally to show the monocrystalline structure of the obtained 70 nm nanorods. The observed lattice spacings 2.50 Å and 2.43 Å correspond well with the calculated spacings of the (311) and (222) spacing (2.53 Å and 2.42 Å) for magnetite and the observed angle between lattice planes of 54.5° also corresponds well with the theoretical dihedral angle between (311) and (Mx0$\bar{0}$31;1Mx0$\bar{0}$31;) of 58° as observed in literature.[60] Thus, the synthesis of monocrystalline nanorods with growth along the [110] axis was successful.

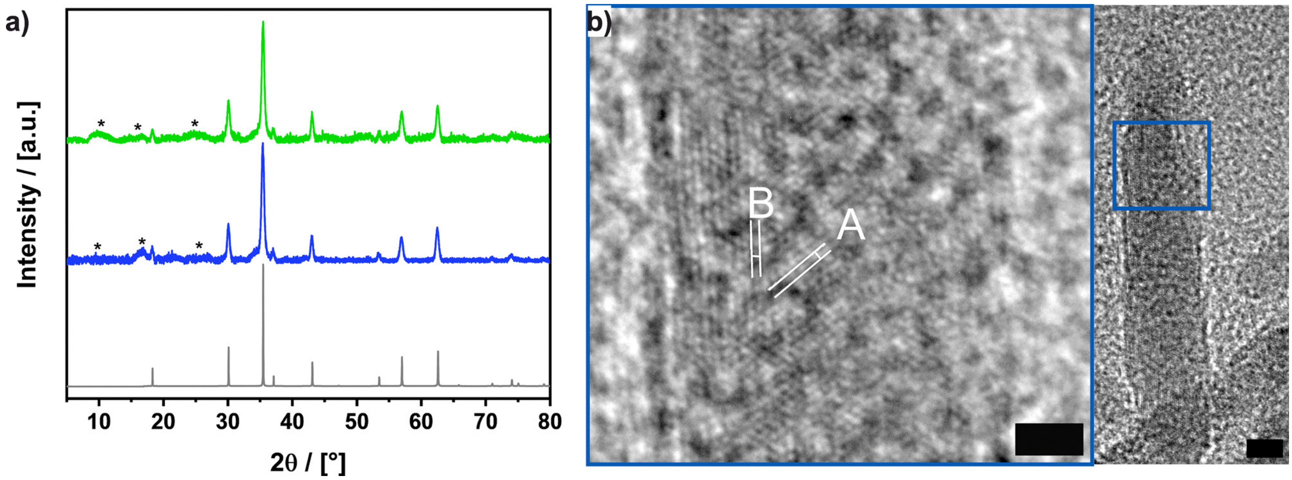

Fig. 2 (a) XRD data of 30 nm nanorods (green) and 70 nm nanorods (blue) and compared to calculated intensities of magnetite using Vesta[59] (grey, cif151330128[58]). Substrate signals are marked with *. XRD data of the other nanorods is shown in Fig. S5. (b) HR-TEM of 70 nm nanorods showcasing the continuous lattice planes indicating monocrystalline nanoparticles (scale bar = 5 nm) with magnification (right, blue box) showing the lattice planes (222) (A, 2.43 Å) and (311) (B, 2.50 Å, scale bar = 2 nm).

The type and presence of the surface ligands were confirmed by using infrared spectroscopy (IR) measurements (Fig. S6 and Table S1). The IR spectra show the characteristic Fe–O stretching vibration of magnetite, along with prominent carboxylate stretching bands (from oleic acid binding) and distinct CH_2 and CH_3 vibrations corresponding to the long-chain hydrocarbons of both the oleic acid and the amine ligands. The observation of the organic content in the obtained nanoparticles by inductively coupled plasma optical emission spectroscopy (ICP-OES, SI A) shows a clear trend: smaller nanoparticles exhibit a reduced ligand weight. This could be either correlated to the weight of the amine, which is lower for smaller nanorods, or to the space needed by oleic acid, which is present on all nanorods Table 1). Overall, the synthesis of magnetite nanorods with different sizes and very similar surface ligand composition was successful, yielding suitable particles for the subsequent assembly procedures.

The conditions for self-assembly experiments using silica-shell free ferrite nanorods are fulfilled, which is described in the next section.

Self-assembly of magnetite nanorods into chain-like superstructures

We applied a similar protocol that led to good results for the assembly of ZnO nanorods in past reports.[9] A nanoparticle dispersion in a volatile, non-polar solvent is placed on top of a viscous, non-volatile polar liquid phase (diethylene glycol). The volatile solvent evaporates, and the concentration of the nanoparticles increases on top of the liquid–liquid interface, ensuring sufficient mobility for the arrangement of the particles into superstructures. The top layer can be removed for isolation and investigation of the formed aggregates. The assembly protocol is shown in Fig. 3a and more details are given in the experimental part. The number of factors that influence the increase of the local nanoparticle concentration due to the evaporation of the top solvent is very large, which influence the nucleation and growth of the nanoparticle-based superstructure. The initial particle concentration, choice of the volatile solvent (cyclohexane in our case), temperature, pressure, type of the surface-bound ligand, the nanorod's aspect ratio, *etc.* have an influence.

We observed that the initial nanoparticle concentration is highly important as it determines how quickly a threshold for nucleation of particle-based superstructures is reached and sufficient initial concentration is needed to form the superstructures. One can observe regions of differing particle density in the samples resulting from differences in the local concentrations during superstructure formation. The nanorods with a length of 30 nm and a width of 5.4 nm (aspect ratio 5.6) are discussed first. Fig. 3 shows a set of TEM micrographs. Drop-casted nanorods are shown in Fig. 3b as reference for extremely low particle densities. As expected, at low particle densities, only small aggregates are forming and the overall orientation of the nanorods can be described as random. Fig. 3c–f show different regions of the samples with increasing local particle densities, obtained using the self-assembly process. At higher local particle density, the parallel alignment of the nanorods begins, which can be observed in Fig. 3c. However, at even higher local concentration (Fig. 3d), elongated structures with higher electronic contrast appear. These structures must correlate to a higher density compared to the surrounding, disordered medium. Interestingly, both phases are composed of 30MagNR, one in a solvent-like (disorder) phase and superchains that have started to nucleate. At even higher particle density (Fig. 3e and f), the length of the superchains grows, and can extend a few micrometers.

An interesting effect is that, similar to polymer gel chemistry, the extended length of the superchains seems to initiate percolation. A network of superchains encloses cavities containing the nanoparticle-based material as a quasi-liquid (Fig. 3f).

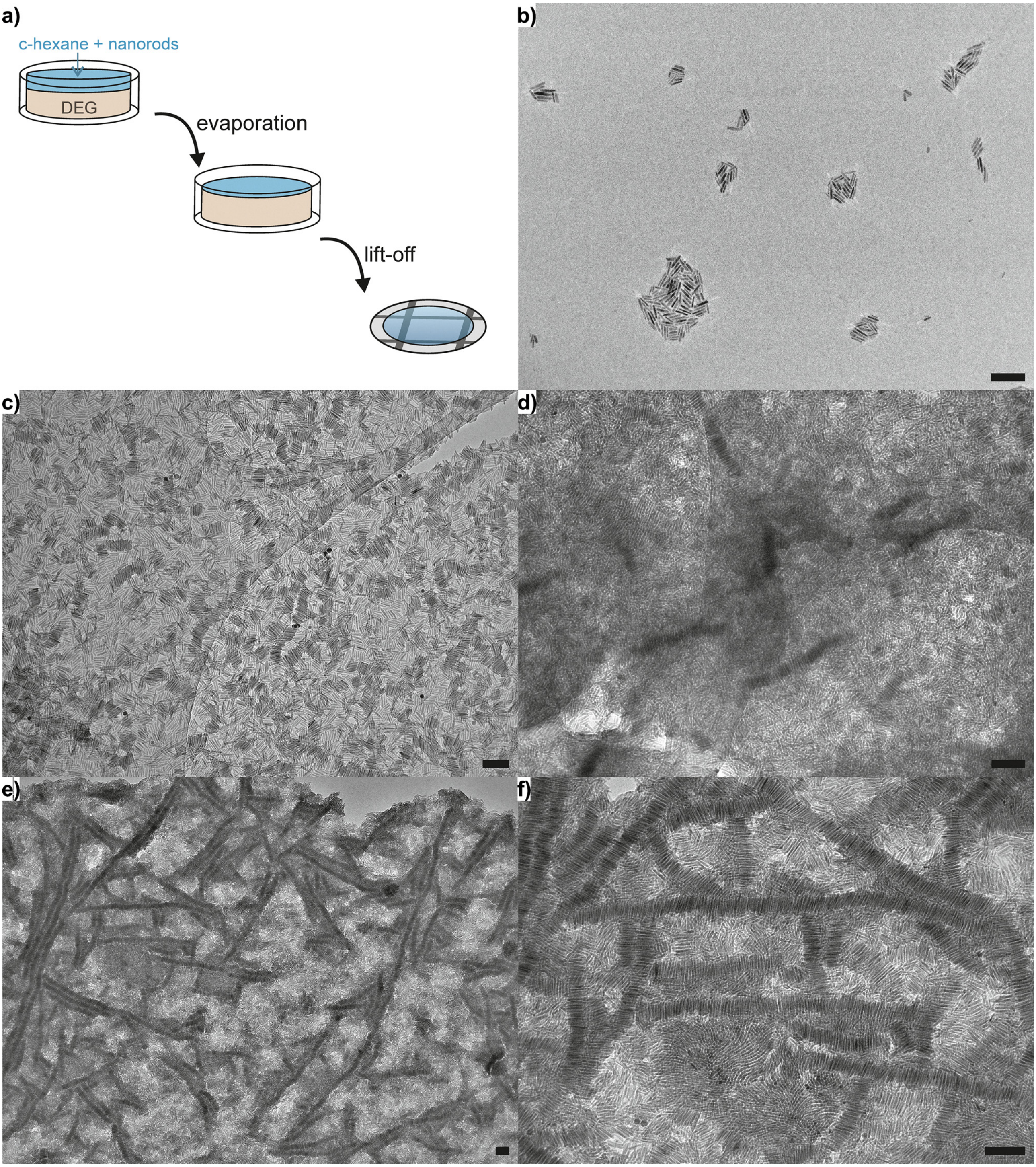

Fig. 3 (a) Scheme of the assembly process, (b) dropcasted 30MagNR at low particle densities, (c–f) increasing local particle densities in assemblies done at an initial concentration of 0.75 mg mL^{-1} studied by TEM (scale bars = 100 nm).

The nanorods with a length of 70 nm and aspect ratio of 7 are considered next. Overall, a similar behaviour can be found, but there are subtle differences compared to 30MagNR. At very low concentration, one can also observe a disordered phase of randomly distributed nanorods on the substrate's surface; TEM micrographs are given in the SI Fig. S7. The tendency for superchain formation seems to be higher for 70MagNR. When the particle density becomes only slightly higher, one can already see the first ordering processes. Fig. 4a shows a TEM micrograph. One sees that the nanorods start to align parallel to each other, forming short, chain-like structures. At higher particle density, also 70MagNR forms the superchains composed of the single nanorods, ending up in a percolated network (Fig. 4b and c). The 3D structure can additionally be seen

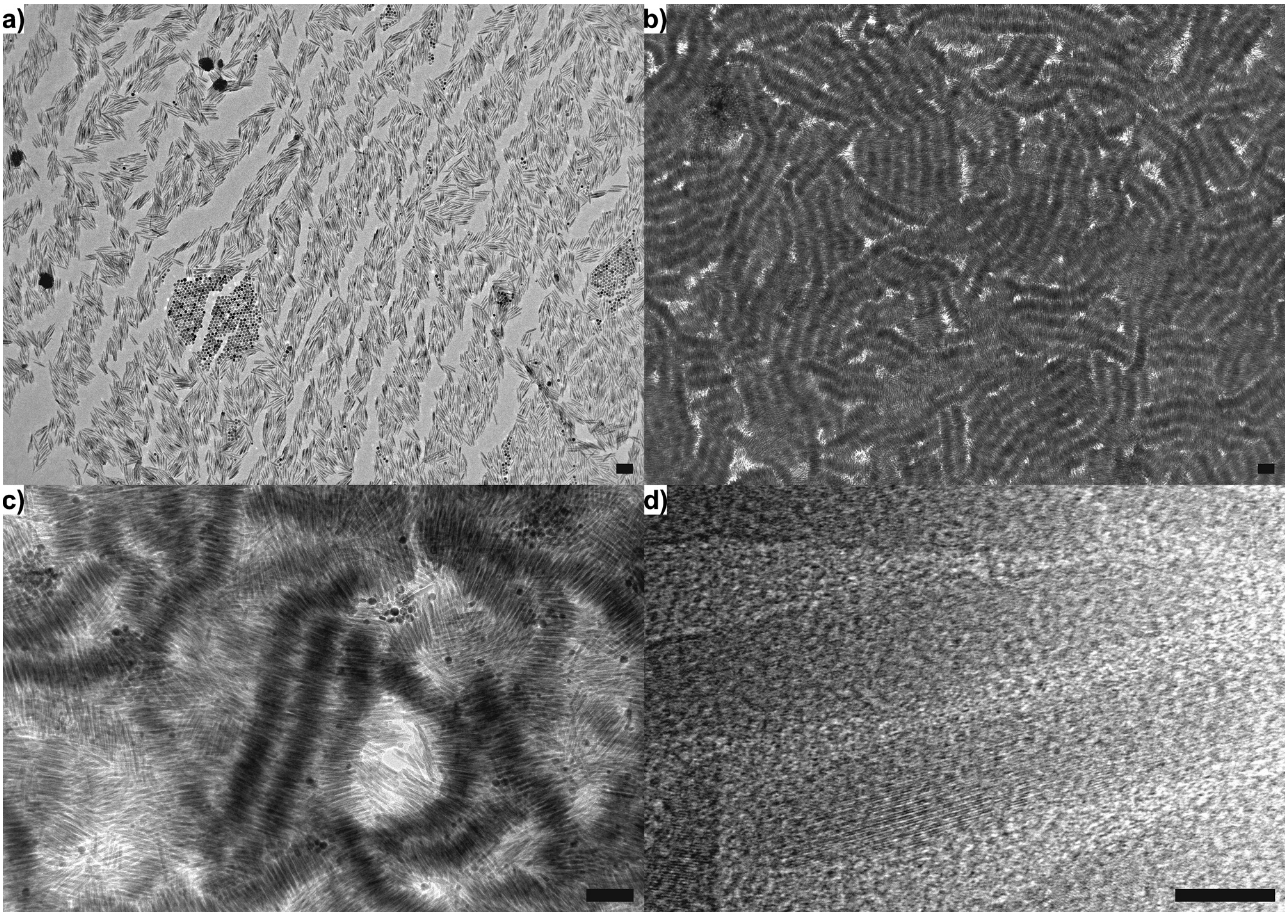

Fig. 4 Assembly modes of 70MagNR with increasing particle density (a), (b and c with scalebar = 100 nm; d with scalebar = 10 nm) studied by TEM.

as investigated by SEM (scanning electron microscopy) in Fig. S8. The fraction of nanorods which are involved in superchain formation is higher compared to the 30MagNR system. The cavities are smaller and filled with less nanorods. Obviously, the longer nanorods can act much less as a quasi-solvent. HR-TEM images (Fig. 4d) provide a realistic value for the distance between closely packed nanorods. The distance of 1.2 nm corresponds to two separating organic ligand layers. It is worth to mention that the observed structure formation can be reproduced using different MagNRs batches (Fig. S9), confirming the higher tendency of 70MagNR to superchain formation and percolation.

The electron microscopy analysis (Fig. 4) shows that indeed, mesophase-like structures with unique structural elements resembling superchains are formed from MagNR, distinct from the typical assembly of non-magnetic nanorods, which mostly form nematic or smectic phases. Longer MagNR seem to have a higher tendency to form such phases. How can one explain the observed assemblies?

The assembly of nanorods from solution is a complex process with a multitude of forces involved including solvent interactions and electrostatic stabilization, ligand interactions, and interparticle interactions.[1] Compared to non-magnetic nanorods, additional magnetic dipole–dipole interactions are present in the system. We have therefore calculated the magnetic dipolar interaction strength present between two adjacent nanorods[63] (SI C). The resulting magnetic coupling parameter Γ for our system, considering the nanorod-nanorod distance observed in the assembly, corresponds to Γ = 114.84 for 70MagNR and Γ = 7.79 for 30MagNR. In both samples the magnetic forces are significantly stronger than thermal fluctuations. This means that once the nanorods approach each other, the magnetic dipolar energy is higher than the thermal energy, leading to the most energetically favourable configuration, which, for side-by-side configuration, is the flux-closing anti-parallel state. As well, as discussed from the magnetic Bjerrum length in SI C, the shorter magnetic nanorods need to be closer together for the dipolar interactions to be dominant, which can additionally explain the observation of shorter and less percolated superchains in this system.

While the interplay of forces during assembly is more complex, in the dried and stabilized superstructures, in the absence of an external magnetic field, the overall magnetostatic energy has to be minimized, which is accomplished by creating a checkerboard structure, as sketched in Fig. 5 (alternating magnetic moments in all directions in the structure).[64] This is supported by the arrangements observed for cobalt nanorods with similar shaped tips. The authors prove that when the tips

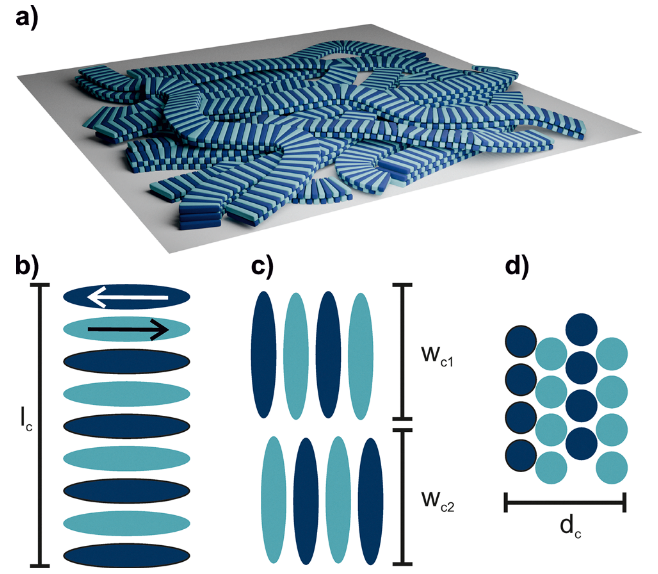

Fig. 5 (a) Idealized architecture of the MagNR-based superchain mesophase-like structure. (b–d) Moment arrangement of a single superchain, highlighting the magnetic dipole interaction (color code indicates the direction of the dipole as shown in (b) within the three directions of the structure to minimize the magnetostatic energy.

of the nanorods are flat, the system assemble in the tip-to-tip configuration where the energy minimization is accomplished by parallel alignment. In contrast, when the tips are rounded, the most stable configuration is the side-by-side with antiparallel moment arrangement, as in our work.[65] Other interesting works on cobalt nanorods arranged in similar side-by-side fashion can be found elsewhere.[66–68] It is important to mention that while these works report the side-by-side assembly of magnetic nanorods, they do not yield superchain structures as the ones observed here.

However, similar superchain motifs have been experimentally reported for CdS[69] and CdSe[70] nanorods, driven by electric dipole–dipole attraction and assisted by surface ligands. Crucially, the assembly protocols are not interchangeable: while simple dropcasting is sufficient in the semiconducting case,[69,70] it leads to random aggregation in our system.

Additionally, recent simulations have also shown that in 2D hard ferromagnetic nanorod structures, densely packed, antiparallelly oriented magnetic moments are the energetically minimal configuration, effectively reducing the overall magnetostatic energy.[59]

Magnetic characterization of the nanorods and assemblies

The establishment of a superstructure composed of ordered ferrimagnetic nanorods prompts the inquiry of how the magnetic properties of the assembly compare to those of the building blocks. For this, we investigated the hysteresis behaviours and temperature dependence using SQUID (superconducting quantum interference device) magnetometry. The results showed that the magnetic properties of the assemblies are very similar to those of single particles, with additional direction-dependency due to the overall anisotropy of the system.

The magnetic properties of the 30 nm and 70 nm nanorods were investigated using SQUID (superconducting quantum interference device) magnetometry. We have performed an in deep investigation of the hysteresis cycles and temperature dependency of the as-synthesized nanoparticles as well as their ordered assemblies, measured in plane and out of plane. Overall, it could be shown that we obtain high-quality magnetite nanorods with saturation magnetization values of around 60 emu g^{-1}. While the particles are close to superparamagnetic behaviour at 300 K as seen in the hysteresis curves in Fig. 6a, the blocking temperature is not reached up to 350 K, suggesting a system in the superparamagnetic–ferrimagnetic limit (blocked regime).[71] Larger nanorods show higher values for the saturation magnetization (M_S) than smaller nanorods corresponding to 74.2% and 68.4% of the bulk value of magnetite (Table S2). The saturation magnetization of both nanorod samples is lower than that of bulk magnetite ($M_S \approx 92$ emu g^{-1})[18] primarily due to surface spin disorder and surface anisotropy, both of which lead to a decrease in overall magnetization.[72] For the shorter nanorods, their slightly lower M_S values are attributed to an increased surface-to-volume ratio, which enhances these surface effects and also contributes to their slightly larger coercivities. At 300 K minor wasp-like behaviour is present in the hysteresis loops associated with the superposition of interacting soft and hard magnetic phases. The measurements shown in Fig. 6a were carried out by drying the samples inside a powder sample holder drop by drop. As this could lead to a preferred orientation of the nanorods and potentially influence the magnetic measurements, we have repeated them with the nanorods distributed in cotton to ensure that no ordering is occurring (Fig. S10). The hysteresis cycles are identical independently of the sample preparation method, so in the powder measurements no preferential orientation is present. The Verwey transition, observed as a distinct kink in the zero-field cooled-field cooled (ZFC-FC) magnetization curve at approximately 120 K (as seen in bulk[18]), provides strong evidence for the presence of stoichiometric magnetite as the main iron oxide phase.[72] All measured samples show the Verwey transition close to 120 K as observed in Fig. 6b, thus further confirming that the main phase of the samples is magnetite. Two other magnetic features can be observed in the thermal dependence of the magnetization, one at lower temperatures around 50 K and another at around 260 K. The small kink observed at lower temperature is frequently associated with the presence of oxygen vacancies,[73] in our case potentially due to the maghemite surface shell formation. However, the exact origin is still under debate, as other works attribute it to magnetic clustering.[74] Moreover, the presence of the second feature at around 260 K, which is around the Morin temperature of hematite,[18] combined with the wasp-waisted loops observed in the hysteresis cycle at 300 K, could indicate the presence of a slightly oxidized surface. As exchange bias at 5 K is present, the coupling between the core–shell phases is confirmed (Fig. S11). Additionally, the blocking temperature is above 350 K and the divergence between the ZFC and

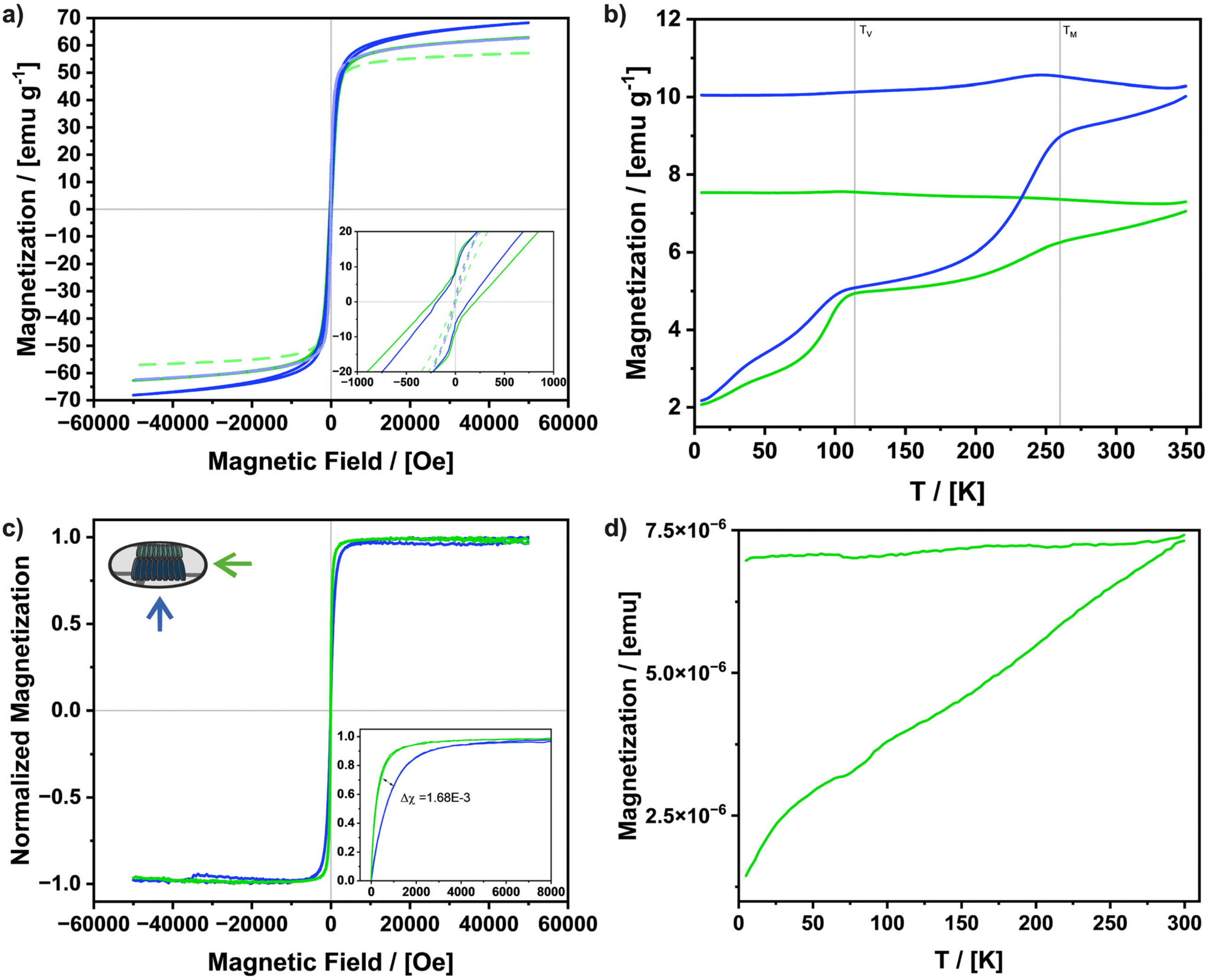

Fig. 6 (a) Hysteresis behaviour of 30 nm nanorods (green) and 70 nm nanorods (blue) at 5 K (continuous line) and 300 K (segmented line) corrected to the amount of magnetite in the sample using the percentages obtained by ICP-OES measurements. (b) Corresponding ZFCFC measurements at 100 Oe. (c) Normalized magnetization of assembled 70 nm nanorods on a Cu TEM grid measured in (green) and out of plane (blue) direction at 300 K. (d) Corresponding ZFCFC measurements at 100 Oe. The substrates used in (c and d) led to an additional magnetization response, thus processing the data to remove substrate contribution was necessary as described in SI B.

FC curves in this high temperature range is indicative of strong interparticle interactions taking place.[75,76] Overall, our nanoparticles show a more complex behaviour than simple superparamagnetism in isolated, non-interacting nanoparticles. The SQUID measurements confirm the quality of our nanorods, with the expected properties of previously reported magnetite nanorods following the solvothermal route.[60] Moreover, these results further confirm the suitability of our versatile synthetic approach, yielding nanoparticles with different lengths but similar aspect ratios.

To investigate the impact of the obtained superstructures from 70MagNR on the direction-dependency of their magnetic properties, the in-plane and out-of-plane hysteresis cycles were recorded at 300 K. It is clearly visible that the assembly is in the superparamagnetic–ferrimagnetic limit similar to its building blocks, as the blocking temperature is not yet reached at 300 K. The susceptibilities observed in the direction-dependent measurements were then compared to a benchmark sample to determine if the anisotropic properties are retained in our superstructures. In the case of the superstructured assemblies, large areas were composed of nanorods oriented perpendicularly towards the surface due to the superchain rotation (Fig. S8-SEM), so the magnetization easy axes of the magnetite nanorods are not simply parallel to the substrate but showcase different angles. The benchmark sample was obtained by dropcasting nanorods onto a substrate in a monolayer and thus provide a reference in which nanorods are perfectly laying parallel to the substrate as seen in Fig. S12a. This is simply due to the shape of the nanorods, which leads to the magnetic easy axis laying in-plane with the substrate (preferred orientation). As can be seen in the hysteresis cycles at 300 K in Fig. 6c and Fig. S12b, the in-plane orientation is favoured in both samples. The susceptibility is significantly higher in in-plane direction compared to random nanorods in powder form, while the out-of-plane susceptibility is lower. To quantify this directional dependence, we have calculated the difference in susceptibility between the in-plane and out of plane orientations ($\Delta\chi = \chi_{\text{in-plane}} - \chi_{\text{out-of-plane}}$), where χ is derived from the initial slope of the normalized magnetization curve (Fig. 6c and Fig. S12b and Table S3). The difference in the susceptibility between in-plane and out of plane measurements is slightly higher in the dropcasted sample, and therefore possessing a higher magnetic anisotropy. This is due to the presence of non-stacked separated nanorods ($\Delta\chi = 2.36 \times 10^{-3}$ Oe^{-1}), which predominantly lie parallel on the substrate, contributing to the in-plane response. Furthermore, the superchain ordered structures exhibit a slightly lower $\Delta\chi$ ($\Delta\chi = 1.68 \times 10^{-3}$ Oe^{-1}), consistent with the observed superchain rotation, while the direction dependent properties are still preserved. The assembled chain like structures were additionally measured at 5 K (Fig. S13), in which the same direction-dependency and close to superparamagnetic behaviour is visible.

Furthermore, the ZFCFC curve was measured in-plane (Fig. 6d). The overall magnetization response is very low due to the low magnetic mass in the assembly, but the VERWEY transition is visible, showing further evidence that the particles are stable during assembly. The ZFCFC curves do not reach the blocking temperature, indicating that high interparticle interactions are also present in the assembled structures.

Overall, the assembled system shows a very similar behaviour to its building blocks, being in the superparamagnetic–ferrimagnetic limit. It is important to note that the proposed checkerboard structure does not require a static, frozen magnetic state to maintain its order. Within the superparamagnetic–ferrimagnetic limit, the magnetic configuration exists in a correlated state where the time-averaged local configuration is driven by strong dipolar interactions. Even as individual moments undergo thermal fluctuations, they do so collectively with their neighbours to minimize the magnetostatic energy. As demonstrated by Durhuus *et al.*,[77] these correlated fluctuations create a magnetic analogue of van der Waals interactions, ensuring that the side-by-side checkerboard motif would remain the energetically favoured structural state even in a system in the superparamagnetic regime. As an advantage in comparison to the individual nanorods, the assembled structures demonstrate good directional dependence, benefitting from the anisotropy of the nanorods.

Methods and experimentals

Used chemicals

Cyclohexane (>99.5%, p.a., Roth), diethyleneglycol (>99%, Sigma Aldrich), dodecylamine (>99%, Sigma Aldrich), ethanol (>99.8, p.a., Roth), hexadecylamine (>94%, Sigma Aldrich), ICP standard solution (ROTI©Star 10 000 mg L^{-1} Fe, Carl Roth), Iron pentacarbonyl (99%, Merck), 1-octanol (99%, thermo scientific), octylamine (99%, Sigma Aldrich), oleic acid (>90%, Sigma Aldrich), oleylamine (>70%, Sigma Aldrich), propylamine (98%, Sigma Aldrich)

Table 2 Used amines for magnetite nanorod synthesis and resulting size

Used amine	Amount [0.82 mmol]	Length/ [nm]	Width/ [nm]	Aspect ratio
Hexadecylamine	200 mg	71.57 ± 0.53	9.99 ± 0.12	7.03 ± 0.16
Dodecylamine	152 mg	33.83 ± 2.19	5.00 ± 0.23	6.41 ± 0.46
Octylamine	136 μL	30.16 ± 2.13	4.59 ± 0.14	6.20 ± 0.15
Propylamine	114 μL	22.29 ± 0.87	3.59 ± 0.02	6.07 ± 0.11
Oleylamine	270 μL	31.41 ± 1.08	5.45 ± 0.11	5.59 ± 0.20

Synthesis of magnetite nanorods

The amine (0.82 mmol, see Table 2) and oleic acid (2 mL, 6.3 mmol) are dissolved in octanol (8 mL) at 55 °C for 30 minutes. After the solution was cooled down to room temperature, iron pentacarbonyl (2 mL, 14.8 mmol) was added and stirred for 10 minutes. The resulting orange solution was added to a Teflon-lined autoclave and heated to 200 °C for 6 hours.

The particles were then precipitated using ethanol (20 mL) and redispersed using cyclohexane (8 mL) and centrifuged (13 416 rcf) three times in this way to clean excess ligand. The nanoparticles were stored dispersed in cyclohexane (8 mL).

Assembly of magnetite nanorods

The assembly is based on previously reported assembly processes,[9,37] and the scheme can be found in Fig. 3a. The magnetite particles were dispersed in a volatile solvent (cyclohexane, 0.4 mg mL^{-1} for 70 nm nanorods and 0.75 mg mL^{-1} for 30 nm nanorods) using ultrasonication and oleic acid (0.5% of solvent volume) was added. Then 400 μL of the obtained solution were carefully overlayered over a non-volatile solvent (diethylenglycol, 2 mL) in a small Petri dish (d = 2.5 cm) and covered. The volatile solvent was slowly evaporated overnight and the obtained assemblies were removed by lifting up a substrate and dried in reduced pressure for at least 24 hours.

ICP-OES measurements

Magnetite nanorods were dried and around 2 mg were digested in 1 mL concentrated aqua regia overnight. The resulting solutions were diluted to obtain solutions inside the calibrated range using reference solutions. Further details are given in SI A.

SQUID measurements

For powder measurements, magnetite nanorods in solution were dried dropwise directly into a powder sample holder and pressed down. Random oriented samples were obtained by drying a drop of magnetite nanorods in cotton, which was then put into a gelatine capsule for measurements. Measurement of substrates were done by attaching the substrate with Kapton tape to an in-plane or out-of-plane substrate holder respectively. Further details are given in SI B.

Used instruments

TEM images were obtained using a Hitachi HT7800 and image were obtained using Radius as well as a FEI Tecnai G2 F20 TMP using Digital Micrograph. SEM images were obtained using a Hitachi Regulus SU8200. Image J was used for size determination for all electron microscope images. XRD spectra were obtained on a Bruker Discover D8 and spectra were generated and background corrected using DIFFRAC.SUITE. Vesta[78] was used to calculate theoretical XRD spectra. ICP-OES data were obtained on a Varian Vista AX using the software ICP Expert II. XPS data was obtained on a PHI Versaprobe III Scanning ESCA and fitted with MultiPak. SQUID measurements were obtained on Quantum Design MPMS3. IR data was obtained on a Bruker VERTEX 70v using OPUS. All other analysis and all graphic representation were done using Origin 2025, Blender and CorelDraw 2024.

Conclusions

In this work, we were able to prepare self-assembled structures of magnetite nanorods, which form ordered superchains composed of nanorods in a side-by-side configuration. We were able to achieve this by fine-tuning a liquid–liquid evaporation protocol, which can be modified to obtain the same structural motif for smaller nanorods. For that, we prepare high-quality and highly controllable magnetite nanorods using a modified solvothermal synthesis approach. Hereby, it could be shown that the length of the carbon chain of the amine used in the synthesis can be directly correlated to the obtained size of the magnetite nanorods. We have characterized the magnetic properties in-depth and could show that the anisotropy of the nanorods can be used to obtain direction-dependent magnetic responses in the assembled structures, retaining the overall magnetic properties of the building blocks. The magnetite nanorods assemble into superchain networks in the absence of an external magnetic field and with no need of silica shells. The self-assembly of monocrystalline magnetite nanorods into percolated superchains is dictated by a complex interplay of forces. Calculations of the interparticle dipolar interaction energy yield values around 10 and 100 k_BT. These energies significantly exceed thermal fluctuations at room temperature, suggesting that magnetic dipolar forces act as the stabilizing factor for the final moment configuration. The resulting flux-closed magnetic configuration (the checkerboard arrangement) minimizes the magnetostatic energy of the overall system.

Experimentally obtaining ordered structures for a ferrimagnetic system opens a variety of perspectives towards switchability of the moments forced by a magnetic field after the structure has been fixed through drying processes.

To the best of our knowledge, this is the first report of obtaining chain-like ordered self-assembled superstructures of magnetite nanorods with high direction-dependent magnetic properties. This is offering potential perspectives towards magnetoelectric applications without the use of insulating shells and where performance relies on the precisely controlled, direction-dependent magnetic properties.

Author contributions

Madeleine Alexandra Schaefer: synthesis, investigation, data curation, formal analysis, writing – original draft, writing – review and editing, conceptualization; Sebastian Polarz: supervision, funding acquisition, project administration, writing – original draft, writing – review and editing, conceptualization; Irene Morales: formal analysis, supervision, project administration, writing – original draft, writing – review and editing, conceptualization.

Conflicts of interest

There are no conflicts to declare.

Abbreviations

AR	Aspect ratio
HR-TEM	High resolution transmission electron microscopy
ICP-OES	Inductively coupled plasma optical emission spectroscopy
IR	Infrared spectroscopy
MagNP	Magnetite nanoparticles
MagNR	Magnetite nanorods
SEM	Scanning electron microscopy
SQUID	Superconducting quantum interference device
TEM	Transmission electron microscopy
XPS	X-ray photoelectron spectroscopy
XRD	X-ray diffraction
ZFCFC	Zero field cooled - field cooled.

Data availability

The authors state that the data supporting the results of this study can be found within the paper and its supplementary information (SI). If raw data is required, it can be provided by the corresponding author upon reasonable request. Supplementary information (SI): additional figures and information regarding the magnetite nanorods synthesis and assembly process are provided in the SI, as well as further details of the ICP-OES and SQUID measurements and calculations. See DOI: https://doi.org/10.1039/d5ma01195g.

Acknowledgements

The authors wish to thank Dr Andreas Schaate (Insitute of inorganic chemistry, Leibniz University Hannover) for measuring XPS and Oliver Jeske (Insitute of inorganic chemistry, Leibniz University Hannover) for providing the IR data. I. M. acknowledges the financial support of the Caroline Herschel Program from the Hochschulbüro für Chancenvielfalt, Leibniz University Hannover. We thank the German Research Foundation (Deutsche Forschungsgemeinschaft, DFG, INST 187/782-1 and Phoenix D, EXC 2122) for funding. The authors wish to thank the Laboratory of Nano and Quantum Engineering (LNQE) of Leibniz Universität Hannover for the access to the TEM facilities. All other analytical measurements were performed in the central analytical facility cf-MATCH of the Leibniz University Hannover.

References

1 M. A. Boles, M. Engel and D. V. Talapin, *Chem. Rev.*, 2016, **116**, 11220–11289.

2 C. Hou, Z. Chen, Z. Chang and L.-T. Yan, *Next Nanotechnol.*, 2025, **8**, 100185.

3 S. Singamaneni, V. N. Bliznyuk, C. Binek and E. Y. Tsymbal, *J. Mater. Chem.*, 2011, **21**, 16819–16845.

4 F. Lübkemann-Warwas, I. Morales and N. C. Bigall, *Small Struct.*, 2023, **4**, 2300062.

5 X. Ye, L. Jin, H. Caglayan, J. Chen, G. Xing, C. Zheng, V. Doan-Nguyen, Y. Kang, N. Engheta, C. R. Kagan and C. B. Murray, *ACS Nano*, 2012, **6**, 2804–2817.

6 S. N. Hosseini, A. Grau-Carbonell, A. G. Nikolaenkova, X. Xie, X. Chen, A. Imhof, A. van Blaaderen and P. J. Baesjou, *Adv. Funct. Mater.*, 2020, **30**, 2005491.

7 B. T. Diroll, N. J. Greybush, C. R. Kagan and C. B. Murray, *Chem. Mater.*, 2015, **27**, 2998–3008.

8 M. Gerigk, J. Bahner, T. Kollek, S. Helfrich, R. Rosenberg, H. Cölfen and S. Polarz, *Part. Part. Syst. Charact.*, 2017, **34**, 1600215.

9 S. Theiss, M. Voggel, H. Kuper, M. Hoermann, U. Krings, P. Baum, J. A. Becker, V. Wittmann and S. Polarz, *Adv. Funct. Mater.*, 2021, **31**, 2009104.

10 D. Baranov, A. Fiore, M. van Huis, C. Giannini, A. Falqui, U. Lafont, H. Zandbergen, M. Zanella, R. Cingolani and L. Manna, *Nano Lett.*, 2010, **10**, 743–749.

11 K. Thorkelsson, P. Bai and T. Xu, *Nano Today*, 2015, **10**, 48–66.

12 P. F. Damasceno, M. Engel and S. C. Glotzer, *Science*, 2012, **337**, 453–457.

13 K. Deng, Z. Luo, L. Tan and Z. Quan, *Chem. Soc. Rev.*, 2020, **49**, 6002–6038.

14 Q. Fan, Z. Li, C. Wu and Y. Yin, *Precis. Chem.*, 2023, **1**, 272–298.

15 S. Chandra, R. Das, V. Kalappattil, T. Eggers, C. Harnagea, R. Nechache, M.-H. Phan, F. Rosei and H. Srikanth, *Nanoscale*, 2017, **9**, 7858–7867.

16 Z. Li, C. Qian, W. Xu, C. Zhu and Y. Yin, *Sci. Adv.*, 2021, **7**, eabh1289.

17 P. Tierno, *Phys. Chem. Chem. Phys.*, 2014, **16**, 23515–23528.

18 J. M. D. Coey, *Handbook of Magnetism and Magnetic Materials*, Springer, Cham, 2021, pp. 1–76.

19 M. D. Nguyen, H.-V. Tran, S. Xu and T. R. Lee, *Appl. Sci.*, 2021, **11**, 11301.

20 Z. Zhou, X. Zhu, D. Wu, Q. Chen, D. Huang, C. Sun, J. Xin, K. Ni and J. Gao, *Chem. Mater.*, 2015, **27**, 3505–3515.

21 C. Lanz, N. Künnecke, Y. Krysiak and S. Polarz, *Nanoscale*, 2024, **16**, 15358–15365.

22 C. Lanz, Y. Krysiak, X. Liu, M. Hohgardt, P. J. Walla and S. Polarz, *Small*, 2023, **19**, 2304380.

23 C. Lanz, M. Schlötter, N. Klinkenberg, P. Besirske and S. Polarz, *Angew. Chem., Int. Ed.*, 2020, **59**, 8902–8906.

24 S. M. Dadfar, K. Roemhild, N. I. Drude, S. von Stillfried, R. Knüchel, F. Kiessling and T. Lammers, *Adv. Drug Delivery Rev.*, 2019, **138**, 302–325.

25 L. Mohammed, H. G. Gomaa, D. Ragab and J. Zhu, *Particuology*, 2017, **30**, 1–14.

26 J. Kim, H. S. Kim, N. Lee, T. Kim, H. Kim, T. Yu, I. C. Song, W. K. Moon and T. Hyeon, *Angew. Chem., Int. Ed.*, 2008, **47**, 8438–8441.

27 R. K. Sharma, S. Dutta, S. Sharma, R. Zboril, R. S. Varma and M. B. Gawande, *Green Chem.*, 2016, **18**, 3184–3209.

28 M. Munoz, Z. M. de Pedro, J. A. Casas and J. J. Rodriguez, *Appl. Catal., B*, 2015, **176–177**, 249–265.

29 M. B. Gawande, P. S. Branco and R. S. Varma, *Chem. Soc. Rev.*, 2013, **42**, 3371–3393.

30 S. C. N. Tang and I. M. C. Lo, *Water Res.*, 2013, **47**, 2613–2632.

31 Y. Zhang, L. Sun, Y. Fu, Z. C. Huang, X. J. Bai, Y. Zhai, J. Du and H. R. Zhai, *J. Phys. Chem. C*, 2009, **113**, 8152–8157.

32 I. Morales, R. Costo, N. Mille, J. Carrey, A. Hernando and P. de la Presa, *Nanoscale Adv.*, 2021, **3**, 5801–5812.

33 K. Simeonidis, M. P. Morales, M. Marciello, M. Angelakeris, P. de la Presa, A. Lazaro-Carrillo, A. Tabero, A. Villanueva, O. Chubykalo-Fesenko and D. Serantes, *Sci. Rep.*, 2016, **6**, 38382.

34 T. Wen and S. A. Majetich, *ACS Nano*, 2011, **5**, 8868–8876.

35 H. Yuan, I. J. Zvonkina, A. M. Al-Enizi, A. A. Elzatahry, J. Pyun and A. Karim, *ACS Appl. Mater. Interfaces*, 2017, **9**, 11290–11298.

36 H. Qi, Q. Chen, M. Wang, M. Wen and J. Xiong, *J. Phys. Chem. C*, 2009, **113**, 17301–17305.

37 G. Singh, H. Chan, A. Baskin, E. Gelman, N. Repnin, P. Král and R. Klajn, *Science*, 2014, **345**, 1149–1153.

38 J. Schlotheuber né Brunner, B. Maier, S. L. J. Thomä, F. Kirner, I. A. Baburin, D. Lapkin, R. Rosenberg, S. Sturm, D. Assalauova, J. Carnis, Y. Y. Kim, Z. Ren, F. Westermeier, S. Theiss, H. Borrmann, S. Polarz, A. Eychmüller, A. Lubk, I. A. Vartanyants, H. Cölfen, M. Zobel and E. V. Sturm, *Chem. Mater.*, 2021, **33**, 9119–9130.

39 A. Chumakova, T. Steegemans, I. A. Baburin, A. Mistonov, I. S. Dubitskiy, J. Schlotheuber, F. Kirner, S. Sturm, A. Lubk, K. Müller-Caspary, I. Wimmer, M. Fonin, E. V. Sturm and A. Bosak, *Adv. Mater.*, 2023, **35**, 2207130.

40 J. Brunner, I. A. Baburin, S. Sturm, K. Kvashnina, A. Rossberg, T. Pietsch, S. Andreev, E. Sturm (née Rosseeva) and H. Cölfen, *Adv. Mater. Interfaces*, 2017, **4**, 1600431.

41 S. Mehdizadeh Taheri, M. Michaelis, T. Friedrich, B. Förster, M. Drechsler, F. M. Römer, P. Bösecke, T. Narayanan, B. Weber, I. Rehberg, S. Rosenfeldt and S. Förster, *Proc. Natl. Acad. Sci. U. S. A.*, 2015, **112**, 14484–14489.

42 L. Li, Y. Yang, J. Ding and J. Xue, *Chem. Mater.*, 2010, **22**, 3183–3191.

43 A. G. Roca, L. Gutiérrez, H. Gavilán, M. E. Fortes Brollo, S. Veintemillas-Verdaguer and M. del P. Morales, *Adv. Drug Delivery Rev.*, 2019, **138**, 68–104.

44 J. Wang, Z. Peng, Y. Huang and Q. Chen, *J. Cryst. Grow.*, 2004, **263**, 616–619.

45 H. Karami, *Chem. Eng. J.*, 2013, **219**, 209–216.

46 S. Chen, J. Feng, X. Guo, J. Hong and W. Ding, *Mater. Lett.*, 2005, **59**, 985–988.

47 S. Geng, H. Yang, X. Ren, Y. Liu, S. He, J. Zhou, N. Su, Y. Li, C. Xu, X. Zhang and Z. Cheng, *Chem. – Asian J.*, 2016, **11**, 2996–3000.
48 O. Bomati-Miguel, A. F. Rebolledo and P. Tartaj, *Chem. Commun.*, 2008, 4168–4170.
49 J. Mohapatra, M. Xing, J. Beatty, J. Elkins, T. Seda, S. R. Mishra and J. P. Liu, *Nanotechnology*, 2020, **31**, 275706.
50 M. Adhikari, E. Echeverria, G. Risica, D. N. McIlroy, M. Nippe and Y. Vasquez, *ACS Omega*, 2020, **5**, 22440–22448.
51 S. Zhang, W. Wu, X. Xiao, J. Zhou, F. Ren and C. Jiang, *Nanoscale Res. Lett.*, 2011, **6**, 89.
52 T. Sen and I. J. Bruce, *Microporous Mesoporous Mater.*, 2009, **120**, 246–251.
53 K. Aguilar-Arteaga, J. A. Rodriguez and E. Barrado, *Anal. Chim. Acta*, 2010, **674**, 157–165.
54 J. A. Marins, T. Montagnon, H. Ezzaier, Ch Hurel, O. Sandre, D. Baltrunas, K. Mazeika, A. Petrov and P. Kuzhir, *ACS Appl. Nano Mater.*, 2018, **1**, 6760–6772.
55 S. E. Favela-Camacho, E. J. Samaniego-Benitez, A. Godinez-Garcia, L. M. Aviles-Arellano and J. Francisco Perez-Robles, *Colloids Surf., A*, 2019, **574**, 29–35.
56 W. Zhang, S. Jia, Q. Wu, J. Ran, S. Wu and Y. Liu, *Mater. Lett.*, 2011, **65**, 1973–1975.
57 T. Ding, K. Song, K. Clays and C.-H. Tung, *Adv. Mater.*, 2009, **21**, 1936–1940.
58 D. Hoffelner, M. Kundt, A. M. Schmidt, E. Kentzinger, P. Bender and S. Disch, *Faraday Discuss.*, 2015, **181**, 449–461.
59 M. A. Dorsey and C. K. Hall, *Langmuir*, 2025, **41**, 3938–3950.
60 H. Sun, B. Chen, X. Jiao, Z. Jiang, Z. Qin and D. Chen, *J. Phys. Chem. C*, 2012, **116**, 5476–5481.
61 K. Nader, I. Castellanos-Rubio, I. Orue, D. Iglesias-Rojas, A. Barón, I. Gil de Muro, L. Lezama and M. Insausti, *J. Solid State Chem.*, 2022, **316**, 123619.
62 F. F. Ferreira, E. Granado, W. J. Carvalho, S. W. Kycia, D. Bruno and R. J. Droppa, *J. Synchrotron Radiat.*, 2006, **13**, 46–53.
63 J. Faraudo, J. S. Andreu and J. Camacho, *Soft Matter*, 2013, **9**, 6654–6664.
64 D. Lisjak and A. Mertelj, *Prog. Mater. Sci.*, 2018, **95**, 286–328.
65 H. Du, M. Zhang, K. Yang, B. Li and Z. Ma, *Nanomaterials*, 2022, **12**, 2499.
66 F. Dumestre, B. Chaudret, C. Amiens, M. Respaud, P. Fejes, P. Renaud and P. Zurcher, *Angew. Chem., Int. Ed.*, 2003, **42**, 5213–5216.
67 F. Wetz, K. Soulantica, M. Respaud, A. Falqui and B. Chaudret, *Mater. Sci. Eng. C*, 2007, **27**, 1162–1166.
68 F. Dumestre, B. Chaudret, C. Amiens, M.-C. Fromen, M.-J. Casanove, P. Renaud and P. Zurcher, *Angew. Chem., Int. Ed.*, 2002, **41**, 4286–4289.
69 A. Singh, R. D. Gunning, S. Ahmed, C. A. Barrett, N. J. English, J.-A. Garate and K. M. Ryan, *J. Mater. Chem.*, 2012, **22**, 1562–1569.
70 A. Singh, R. D. Gunning, A. Sanyal and K. M. Ryan, *Chem. Commun.*, 2010, **46**, 7193–7195.
71 I. J. Bruvera, P. Mendoza Zélis, M. Pilar Calatayud, G. F. Goya and F. H. Sánchez, *J. Appl. Phys.*, 2015, **118**, 184304.
72 A. Mitra, J. Mohapatra and M. Aslam, *Mater. Res. Express*, 2024, **11**, 022002.
73 L.-Y. Zhang, D.-S. Xue, X.-F. Xu and A.-B. Gui, *J. Magn. Magn. Mater.*, 2005, **294**, 10–15.
74 D. González-Alonso, J. González, H. Gavilán, J. Fock, L. Zeng, K. Witte, P. Bender, L. Fernández Barquín and C. Johansson, *RSC Adv.*, 2021, **11**, 390–396.
75 M. Ounacer, A. Essoumhi, M. Sajieddine, A. Razouk, B. F. O. Costa, S. M. Dubiel and M. Sahlaoui, *J. Supercond. Novel Magn.*, 2020, **33**, 3249–3261.
76 H. Hu, Y. Yuan, S. Lim and C. H. Wang, *Mater. Des.*, 2020, **185**, 108241.
77 F. L. Durhuus, M. Beleggia and C. Frandsen, *J. Phys. Chem. C*, 2026, **130**, 2696–2708.
78 K. Momma and F. Izumi, *J. Appl. Crystallogr.*, 2011, **44**, 1272–1276.